Materials and Design 198 (2021) 109381

Contents lists available at ScienceDirect

Materials and Design

journal homepage: www.elsevier.com/locate/matdes

Programmable shape-shifting 3D structures via frontal photopolymerization

Jinqiang Wang[a], Ning Dai[b], Chengru Jiang[a], Xiaoming Mu[d], Biao Zhang[e], Qi Ge[c], Dong Wang[a,*]

[a] *Robotics Institute and State Key Laboratory of Mechanical System and Vibration, School of Mechanical Engineering, Shanghai Jiao Tong University, Shanghai 200240, PR China*
[b] *School of Mechanical and Electrical Engineering, Nanjing University of Aeronautics and Astronautics University, Nanjing 210016, PR China*
[c] *Department of Mechanical and Energy Engineering, Southern University of Science and Technology, Shenzhen 518055, PR China*
[d] *Department of Mechanical Engineering, Wilkes University, PA 18701, USA*
[e] *Xi'an Institute of Flexible Electronics and Xi'an Key Laboratory of Biomedical Materials & Engineering, Northwestern Polytechnical University, Xi'an 710072, Shaanxi, PR China*

HIGHLIGHTS

- The shape-shifting behaviors from 2D polymer films to 3D structures via FPP are studied.
- A combined theoretical, experimental and numerical model is proposed to capture the shape-shifting phenomenon.
- Elastic instability in the shape transition is captured using the minimization of the elastic energy.
- Various 3D structures are designed by using grayscale light patterns.

GRAPHICAL ABSTRACT

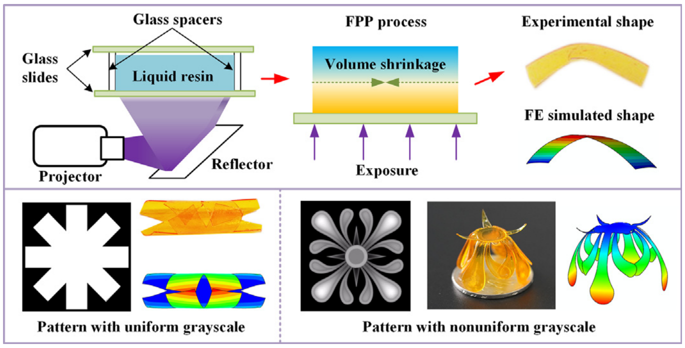

ARTICLE INFO

Article history:
Received 14 September 2020
Received in revised form 2 December 2020
Accepted 2 December 2020
Available online 07 December 2020

Keywords:
Programmable shape-shifting
Frontal photopolymerization
Elastic instability
Edge effect
Grayscale patterning

ABSTRACT

Shape-shifting structures have gained growing interest recently and found wide applications in areas such as soft robotics, biomedical devices and self-folding origami, attributed to their ability to construct complicated shapes directly from simple structures. However, an efficient method to design and fabricate programmable 3D shape-shifting structures from 2D polymer films still lacks. In this work, we design programmable shape-shifting 3D structures via the release of internal gradient stress using the frontal photopolymerization (FPP) method. First, the relation between the non-uniformly distributed material and loading parameters, and the geometric and fabrication parameters are established theoretically. The finite element (FE) model is then developed based on the theoretically obtained material and loading parameters. Next, the elastic instability in the shape-shifting behaviors of a cured film is captured through an elastic energy minimization. Furthermore, by using grayscale light patterns, it is shown that we can selectively manipulate the geometric and fabrication parameters to improve the design freedom of various complex 3D structures.

1. Introduction

Shape-shifting structures are ubiquitous and have attracted increasing attention due to their wide applications in soft robotics [1], self-folding origami [2,3], and biomedical devices [4–6]. A common way of generating shape-shifting is to utilize the elastic instabilities due to

---

* Corresponding author.
E-mail address: wang_dong@sjtu.edu.cn (D. Wang).

https://doi.org/10.1016/j.matdes.2020.109381

the competition between bending and stretching in response to an external or internal actuation [6–10]. Examples include the twisting of organic molecules [11,12], shedding of wheat awns [13] and folding of pine cones [5,14].

With the increasing demand for reconfigurable objects in engineering and the limitation of the manufacturing methods on producing complex 3D shapes, innovative approaches are proposed recently to form 3D structures [3,15–21]. For instance, inspired by biological structures' morphogenesis, a strategy is proposed to develop controllable and complex shape transformations of elastomer plates under air pressure [22]. The shape transformation of the 2D hydrophilic/hydrophobic composite to 3D structures resulting from the desolvation-induced shrinkage was investigated [18,19,21]. Volumetric strain produced by the anisotropic swelling of an elastic network within a solvent is widely applied to generate complex 3D structures, such as the morphology of growing tissues [23], the blooming of flowers [24] and the delamination of fuel cell membranes [25]. A direct laser writing method is used to create microstructures with programmable self-bending behavior [26]. A mechanical model is presented to predict the bending shapes, which opens prospects for a fast and simple creation of shape morphing structures with complex geometries. Additionally, 4D printing, where the fourth dimension refers to time, are already emerging to build programmable shape-shifting structures in response to the external stimulus by controlling the material distribution and structural parameters [15,27–29].

Another way of forming 3D structures is to use the shape-shifting phenomenon of 2D cured thin films driven by the internal stress using the frontal photopolymerization (FPP) method. In FPP, a polymer film is cured continuously from one side of the liquid resin [3,30,31]. Upon irradiation, the photopolymerization process develops and the solidification front initiates at the surface. With the continuous illumination, the solidification front propagates and invades the uncured resin. In the process of polymerization, the volume decreases resulting from the covalent bond formation. Due to the light intensity gradient caused by the photo absorbers, the volume shrinkage occurs sequentially. The light-entering surface layer shrinks freely first and stores neglectable internal stress. Therefore, the first layer can be regarded as in an initial stress-free state [3]. Under the continuous illumination, the subsequently cured layers then shrink under the confinement of the early cured layers. Thus, the polymer film tends to bend toward the newly cured layers.

Due to the constraint of the platform, the cured film remains flat with non-uniform built-in stress. Once the structure is removed from the platform, the released internal stress transforms the 2D film to a 3D structure. Recently, this previously undesired phenomenon is found useful to fabricate 3D origami structures [3,20,21]. However, the structures chosen to be cured and then bent in the 2D film are often slender beams with large aspect ratios. Thus, the bending only takes place in one direction, which significantly hurdles the fabrications of complex 3D structures. Compared to the one-dimensional bending of the beam structure, the evolution of a 2D shell into a 3D structure is more complicated because of the two-dimensional bending, large deformation and the instability caused by the competition between stretching and bending.

The instability in the transition from a 2D thin film to a 3D structure has been explored by many researchers. For example, Stoney investigated the relation between self-folding and residual stress generated from the isotropic mismatch strain in a bilayer [32]. Freund further revealed the bifurcation of deformation modes from axial symmetry to asymmetry with increasing mismatch strain [33]. Holmes et al. focused on the shape morphing induced by the non-homogenous swelling and provided theoretical guidelines for the bifurcation and isometric limit [34,35]. Abdullah et al. demonstrated that all of the initial shape, structural nonlinearity and edge layer would influence the shape transformation of polygonal bilayers [36–38].

Unlike these works that were investigated from a geometric nonlinearity perspective, some researchers offer insights into the variation of energy during shape-shifting. For example, Carl Modes et al. demonstrated that bifurcation into an approximately singly curved state is energy favorable for thin sheets [39]. Chun et al. observed that the bending direction varies depending on the length to width ratio in the production of micro-scale tubes [40]. Alben et al. further revealed that a lower energy region along the edges causes the rolling in the long direction [41]. However, in the above work, the shape transitions are mainly driven by the mismatch strain in a bilayer. But in frontal photopolymerization, the strain/stress is non-uniformly and continuously distributed along the thickness direction.

Several explorations on FPP have been conducted before [3,30,42–45]. Zhao et al. proposed the formation of origami structures by the FPP method and analyzed the underlying mechanism [3]. The geometrical patterns of the deformable region are mostly hinges with a large aspect ratio, which restricts the bending in only one direction. This method eases the formation of origami structures, but on the other hand, limits the formation of more complex structures.

In this work, we extend the deformable region to various 2D geometrical patterns. To program the 3D structures, a combination of the experimental, theoretical and numerical methods is developed. The non-uniformly distributed material and strain/stress are taken into account. The elastic instability due to the competition between bending and stretching exists in the shape transition and is captured using the proposed model. Finally, by using the grayscale patterning, it is demonstrated that various 3D structures can be designed and fabricated by varying the geometrical parameters and illumination doses.

2. Materials and methods

2.1. Material

This work focuses on the shape-shifting behaviors of 2D polymer sheets induced by the non-uniform volume shrinkage during photopolymerization. The photopolymer resin was prepared by adding the photoinitiator into a mixture of monomer and plasticizer. Sudan I was used as the photo absorber. The monomer Poly (ethylene glycol) diacrylate (i.e., PEGDA, Mn = 700 g/mol, 99.8%) and the plasticizer polyethylene glycol (i.e., PEG, Mn = 400 g/mol, 99.8%) were purchased from Sigma-Aldrich (St. Louis, MO, USA). The role of PEG is to reduce density by occupying intermolecular space between PEGDA during polymerization, resulting in lower conversion and modulus [46,47]. Photoinitiator phenylbis (2,4,6-trimethylbenzoyl) phosphine oxide (Irgacure 819) and photo absorber Sudan I were purchased from Macklin (Shanghai, China). All the chemicals were used in their as-received conditions. The mixture containing 90.23 wt% PEGDA, 9 wt% dispersant PEG, 0.66 wt% Irgacure 819, and 0.11 wt% Sudan I was stirred on the magnetic stirring apparatus (SILE-85-2, China) until a full dissolution of the photoinitiator and photo absorber. We degassed the solution through an ultrasonic cleaner for 5 min before use. The entire process was conducted in a dark environment to avoid undesired polymerization before use.

2.2. Fabrication

A ~ 2 mL drop of photocurable resin was injected into a reaction cell consisting of two quartz glass slides (100 mm × 100 mm × 2 mm) separated by two glass spacers (0.5 mm thick). The pre-treatments of the slides include an ethanol cleaning step followed by substrate coating (PDMS, Sylgard 184, Dow Coming Corporation, 0.2 mm thick). The PDMS coating can reduce the adhesion between the film and the glass slide due to the difference of surface energy between siloxane groups (hydrophobic) and PEGDA (hydrophilic) [48–50]. The reaction cell was placed on a fixed platform positioned at the focal plane of a light projector (DLP LightCrafter 6500, Wintech, China, wavelength 405 nm). A designed grayscale bitmap was projected onto the resin under a given irradiation time. The continuous light triggered the photopolymerization process. The attenuation of the light intensity produced by the photo absorber facilitated the formation of non-uniform polymerization.

After the photopolymerization, we removed the top glass spacer and sucked the excess liquid resin with a straw. We then moved the cured film from the substrate to a piece of absorbing paper gently. Next, we covered another piece of absorbing paper on the cured film for seconds to remove the residual monomers. The cured film was then peeled from the paper and deformed freely on a flat plate. After the shape change due to the internal stress release, many unreacted monomer/solvent remained trapped in the polymeric network. Post-processing was then conducted to cure the unreacted monomers for around 2 min using the near UV light and fixed the deformed shapes. The post-processing significantly increases the modulus of the structures.

2.3. Characterization

The incident light intensity was calibrated using an ultraviolet radiometer (UV-A, SKUNUY, China). To characterize the polymerization ratio in the films, we measured the absorbance spectrum of double bonds using Fourier transform infrared spectroscopy (FTIR) on an FTIR spectrometer (NEXUS670, USA). Mechanical tests were conducted to obtain the Young's modulus. The mass density was measured by the gas hydrometer (TZFM300–2, China). Image processing software ImageJ was introduced for the measurement of curing thickness and bending curvature of films. Details on the experiments can be found in the Supplementary Materials.

3. Results and discussions

3.1. Mechanism of FPP method

Fig. 1a schematically shows the experiment setup of the DLP-based FPP process, where the light is generated by a projector and reflected by a reflector to cure the liquid resin upward from the bottom through a transparent glass slide. Upon illumination, the photoinitiator decomposes into free radicals, and these free radicals react with the polymer

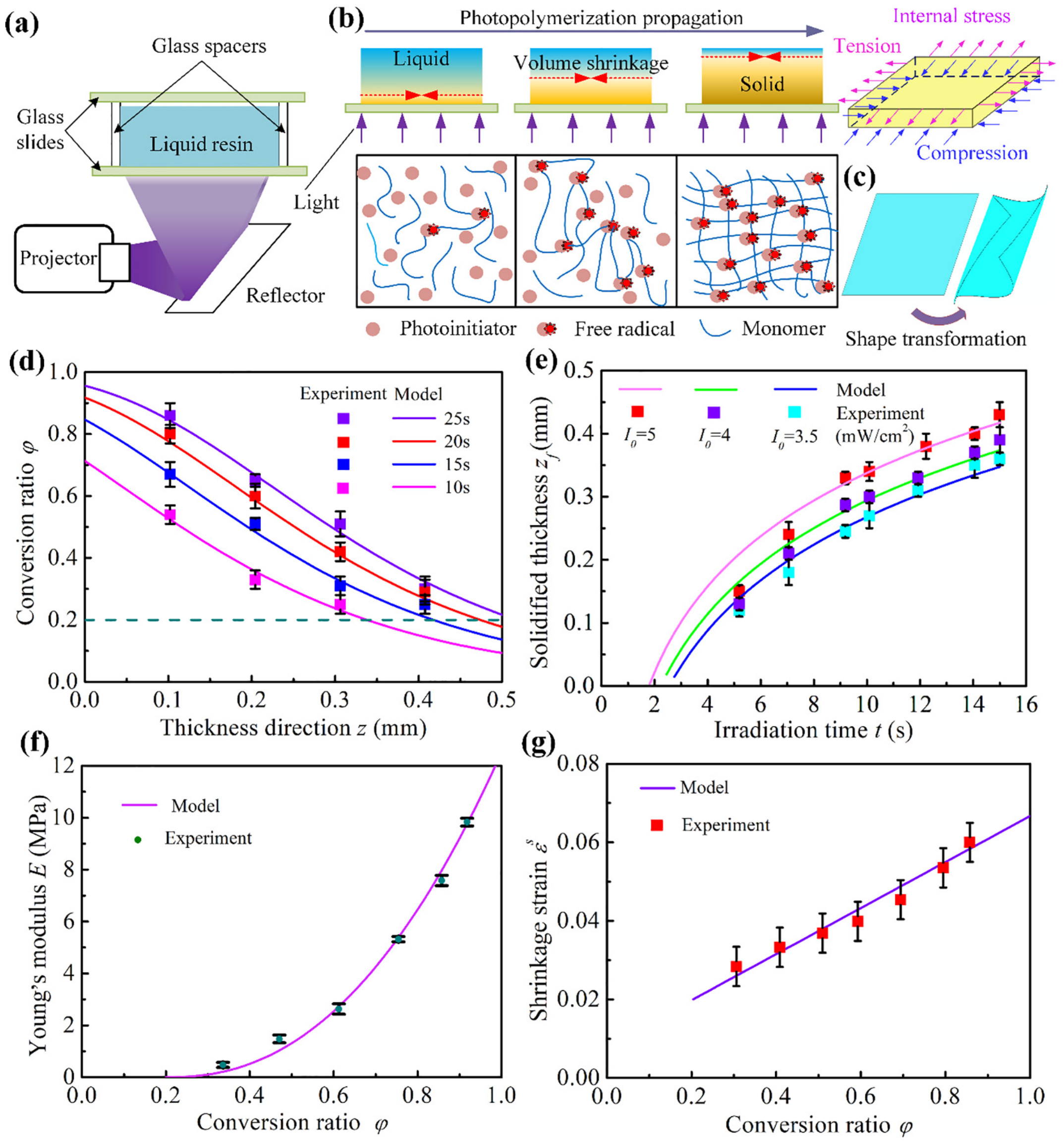

Fig. 1. The shape-shifting behavior of thin film under FPP. (a) Schematic of the DLP-based FPP experiment setup. (b) The front of the solidification interface propagates from the illuminated surface (bottom) into the resin during the process of FPP. The sequential volume shrinkage of the cured layer is due to the formation of the covalent bonds. (c) The cured layer deforms from a 2D to a 3D structure due to internal stress after removed from the substrate. (d) The conversion ratio varies with the distance to the illuminating surface under different exposure doses. The samples were cured under an incident light intensity of 4 mW/cm^2 for 10 s, 15 s, 20 s, and 25 s, respectively. The dashed line represents the critical conversion ratio. (e) The solidified thickness varies as a function of irradiation time. The light intensities used are 3.5, 4, and 5 mW/cm^2, respectively. (f) Young's modulus varies as a function of the conversion ratio. (g) Shrinkage strain changes as a function of the conversion ratio.

monomers to form a larger polymer network (Fig. 1b). The volume decreases during polymerization, resulting from the formation of the covalent bonds. Therefore, the volume shrinkage during FPP is a function of the polymerization ratio.

Upon irradiation, the liquid surface solidifies immediately and the first layer undergoes free volume shrinkage. So, it can be considered as in a stress-free state. The following layers form slowly because of the insufficient illumination blocked by the solidified layers and absorbed by the photo absorber. Due to the volume shrinkage during polymerization, newly formed layers will contract under the constraint of the previously cured layers. Thus, the cured polymer film tends to bend toward the newly formed layers. But it remains a flat shape limited by the substrate. Once it is removed from the substrate, the residual stress inside the polymer film drives it to bend (Fig. 1c and Video S1). To better explain the internal stress formation and the shape transformation mechanism, we use the layer concept to distinguish the early cured part and the newly cured part. However, it should be noted that the film is cured under a single layer printing. To accurately control the internal stress and the resulting shape, a photo absorber is used to enlarge the light intensity gradient. This light intensity gradient will lead to a gradient of the polymerization ratio and generate different contraction ratios along the thickness direction.

3.2. Distribution of mechanical properties and internal stress along z

In this subsection, the non-uniformly distributed mechanical properties, shrinkage strain and internal stress on the thickness direction are obtained.

First, the conversion ratio of the liquid monomer into solid networks φ ($0 \le \varphi \le 1$) along the thickness direction z of the cured film is measured. The origin of the z coordinate is set on the illumination surface of the cured film. The conversion ratios are measured using the FTIR spectra method. The experimental conversion ratios at $z = 0.1$ to 0.4 mm under different illumination times are presented by the markers in Fig. 1d. Noted that the monomer-to-polymer conversion only exits upon a critical threshold conversion φ_c. This conversion ratio φ_c is measured and set as 0.2.

Based on the general Beer-Lambert law, the conversion profile along z-direction can be obtained as [30,31]:

$$\varphi(z,t) = 1 - \exp\left[-KI_0 \exp\left(-\mu_0 z\right)t\right], \tag{1}$$

where t is the irradiation time, K a material-related reaction constant, I_0 the incident light intensity and μ_0 the attenuation coefficient. By comparing the theoretical and experimental φ in Fig. 1d, K and μ_0 are fitted as K=0.025 cm^{2}mW^{-1} s^{-1} and μ_0=5.1 mm^{-1}. At the interface between solid and liquid, the conversion ratio is φ_c. Substituting φ_c into Eq. (1), the corresponding solidified thickness z_f can be written as:

$$z_f = \frac{\ln\left[KI_0 t/\ln\left(1/(1-\varphi_c)\right)\right]}{\mu_0}. \tag{2}$$

In Fig. 1e, the theoretical predicted and experimental measured z_f are compared for samples cured with different times under various light intensities 3.5, 4, and 5 mW/cm^2.

Due to the illumination gradient, the Young's modulus E varies along the thickness direction. We measured E of the cured sample at various φ as shown in the markers in Fig. 1f. An apparent gradient exists within E. The cured layer near the substrate has the largest modulus, while that at the solid-liquid interface shows a vanishing modulus. An exponential function is then used to fit the continuous change of E along z directions [3,20].

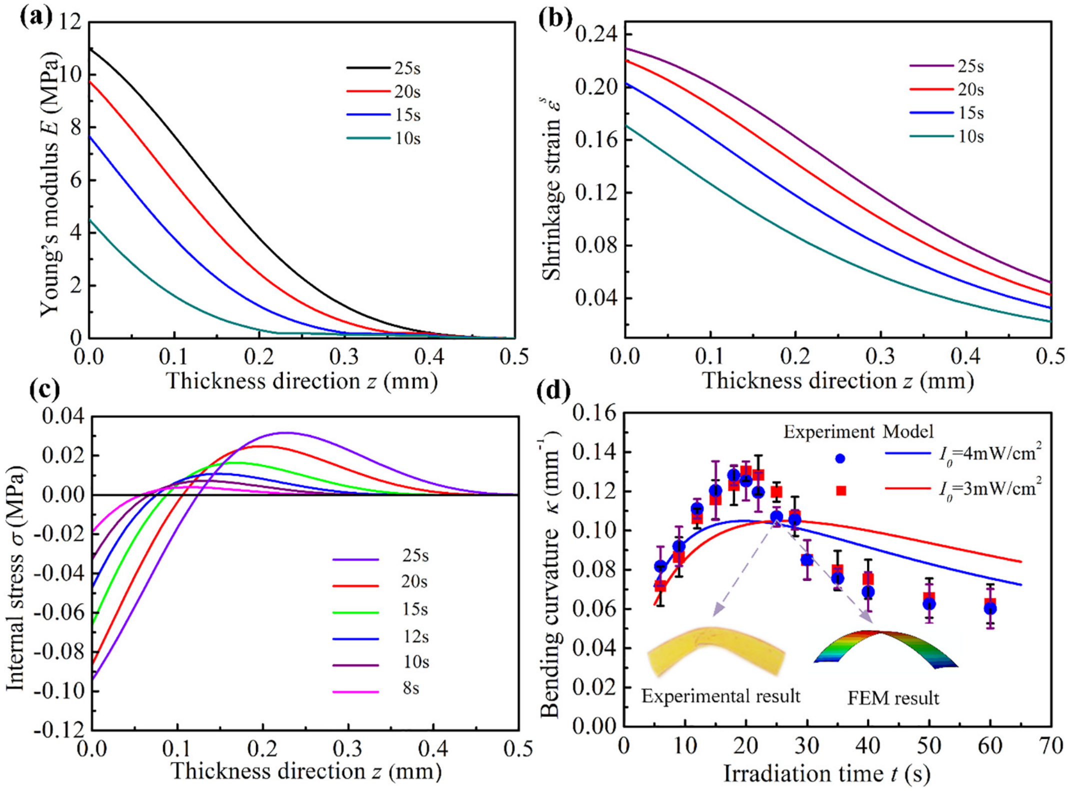

Fig. 2. Mechanical properties of the polymer films cured by FPP. (a) Young's modulus, (b) shrinkage strain, and (c) internal stress vary with the distance to the illuminating surface under different irradiation times. (Incident ultraviolet light intensity is 4 mW/cm^2) (d) Comparison between the experimental and theoretical bending curvatures as a function of irradiation time of one-dimensional cured beam (incident light intensities are 3 (red) and 4 (blue) mW/cm^2). (For interpretation of the references to colour in this figure legend, the reader is referred to the web version of this article.)

$$E(\varphi) = E_0(\varphi - \varphi_c)^{\beta}, \tag{3}$$

where E_0 and β are fitted as E_0=20.9 MPa and β=2.3. By substituting Eq. (1) into Eq. (3), the dependence of E on z can be obtained and is plotted in Fig. 2a for the sample with various curing times.

To obtain the distribution of the shrinkage ratio on the z direction, the shrinkage strain ε^s of the cured film under different exposure doses D (the product of incident light intensity I_0 and irradiation time t, $D = I_0 \times t$) are measured. The dependence of the measured ε^s on φ is plotted in Fig. 1g and fitted by a linear function [3]:

$$\varepsilon^s(\varphi) = \varepsilon^s_{initial} + \left(\varepsilon^s_{final} - \varepsilon^s_{initial}\right)(\varphi - \varphi_c), \quad (\varphi > \varphi_c) \tag{4}$$

where $\varepsilon^s_{initial}$ and ε^s_{final} are fitted as $\varepsilon^s_{initial} = 0.0198$, $\varepsilon^s_{final} = 0.0784$. Substituting Eq. (1) into Eq. (4), the dependence of ε^s on z can be obtained and is plotted in Fig. 2b. Similar to E, ε^s varies significantly along z and can be denoted by $E(z)$ and $\varepsilon(z)$.

Next, the internal stress σ for a cured film is obtained. During photopolymerization, samples remain flat due to the constraints by the substrate. In the flat status, the sample exhibits a uniform total strain ε, which is independent of z. Besides the shrinkage strain ε^s already formed during the photopolymerization, only an in-plane elastic strain ε^m exists. Therefore, ε^m is a function of z and can be written as

$$\varepsilon^m(z) = \varepsilon - \varepsilon^s(z), \tag{5}$$

and the elastic internal stress σ can be written as:

$$\sigma(z) = E(z)\varepsilon^m(z). \tag{6}$$

By substituting Eqs. (1), (3)–(5) into Eq. (6), σ can be written as a function of z and t as:

$$\sigma(z,t) = E_0\left(1 - \exp\left[-KI_0 \exp\left(-\mu_0 z\right)t\right] - \varphi_c\right)^{\beta} \times \\ \left(\varepsilon - \left(\varepsilon^s_{initial} + \left(\varepsilon^s_{final} - \varepsilon^s_{initial}\right)\left(1 - \exp\left[-KI_0 \exp\left(-\mu_0 z\right)t\right] - \varphi_c\right)\right)\right). \tag{7}$$

From the force equilibrium along the curing depth, the following equation can be obtained:

$$\int_0^{z_f} \sigma dz = \int_0^{z_f} E\varepsilon^m dz = 0. \tag{8}$$

By substituting Eq. (7) into Eq. (8), ε can be solved numerically. The distribution of σ along z is shown in Fig. 2c. It can be seen that the early cured layer possesses compressive stress, while the newly cured layer experiences tensile stress. The continuous FPP process is conducted on a substrate, which provides constraints. The constraints from the substrate and the networks formed previously prevent the shrinkage of the newly crosslinked chains. Therefore, the newly crosslinked layers are under tension.

To verify the distribution of σ, experiments for cured beams under different incident light intensity and irradiation time were conducted. When a cured beam with a large aspect ratio is removed from the substrate, the internal stress will drive it to bend. The bending curvatures were measured and compared with the theoretical predictions, as shown in Fig. 2d. The theoretical model is based on the Euler-Bernoulli beam model [51,52], and shown in the Supplementary Materials. Interestingly, both the theoretical and experimental curvatures show a maximum under a moderate exposure dose. With longer irradiation time, the magnitude of the internal stress increases, while the Young's modulus also increases. The competition between the increasing internal stress and increasing Young's modulus leads to a maximum at a moderate exposure dose. Finite element (FE) simulations are also conducted. The theoretical E and ε^m along the $z$direction are discretized into n layers, and the discretized E_i and ε_i ($i = 1$ to n) are given as input in the FE simulations. A composite shell section is used to set E_i and ε_i for the material. We set $n = 8$ in all the simulations. The detailed procedure of FE simulations is provided in the Supplementary Materials. The experimental and FE simulated deformed shapes of a cured beam under 100 mJ/cm^2 are shown in the inset of Fig. 2d.

There are some discrepancies between the model and bending experiments in Fig. 2d. First, the accurate measurement of the curvatures is challenging as the cured strips were not always symmetrically bent. Second, the influence of the thermal strain is neglected in the photopolymerization model. Last, gravity also plays a role in the deformation. Improvement can be made by incorporating the thermal strain and gravity in the model.

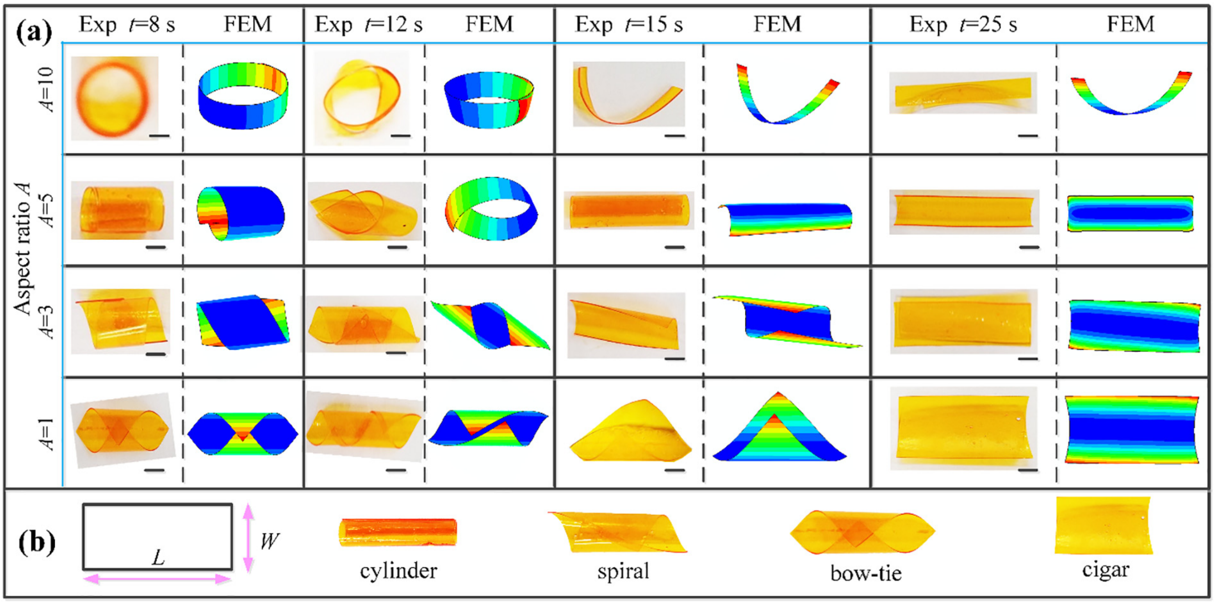

Fig. 3. Deformation of slender structures. (a) The experimental and FEM simulated deformed shapes of the rectangular films with different aspect ratios A under various exposure time t. (b) The four possible deformation modes. All of the scale bars are 3 mm.

3.3. Effect of aspect ratios

The effects of the geometrical parameter (aspect ratio $A = L/W$) and manufacturing parameters (irradiation time t, exposure dose D) are investigated. Experiments were conducted for polymer films with different $A = 1$, 3, 5 and 10 under different irradiation time $t = 8$ s, 12 s, 15 s, 25 s. The incident light intensity used was $I_0 = 4$ mW/cm^2. Several experiments were conducted for each sample with the same geometrical and manufacturing parameters. The deformed shapes that appear with the highest frequencies are shown in Fig. 3a. A thin rectangular film may yield into four possible shapes: a "cigar" (short edge curved), a "cylinder" (long edge curved), a "bowtie" (diagonal curved), or a "spiral" (intermediate angle curved) (shown in Fig. 3b and Video S2). It can be seen from Fig. 3a that at $A = 10$, the cured film tends to bend with respect to the short axis. Its curvature reaches the maximum at $t = 12$ s and decreases as time increases. For a film cured under moderate t (8 s or 12 s), its bending axis rotates from the short axis at $A = 10$ to the diagonal at $A = 1$. The deformed shape changes from a cylinder ($A = 10$) to a spiral ($A = 5$ and 3), and finally to a bowtie at $A = 1$. Under a large t (25 s), the modulus of the cured films is high. Thus, the internal stress is not strong enough to induce large deformation and the deformed shapes are cigars. The corresponding FE simulated deformed shapes are shown beside the experimental shapes.

3.4. Elastic instability in the shape transformation

From Fig. 3, we can observe that the bending axis changes with various A and D. Based on the experimental observations and previous research [9,11,17,33,40,41], there is a bifurcation from spherical to bending shape as the 2D thin film deforms. Thus, the choice between a spherical shape and a bending shape, and the choice of the bending axis remain unknown. To find the preferred shapes, the elastic energies of the various deformed shapes are calculated from FEM simulations and compared.

First, the bifurcation between the spherical and bending shapes is investigated. Fig. 4a plots the total strain energy for the spherical and bending shapes with incremental releasing of the internal stress. The incident light intensity used is 5 mJ/cm^2 and three illumination times $t = 15$, 20 and 25 s are chosen. The bending is assumed to be with respect to the axis with $\theta = 0°$, where θ is the angle between the bending axis and the vertical direction, as shown in the inset of Fig. 4b. It can be seen that the energy of the spherical shape is less than that of the bending shape

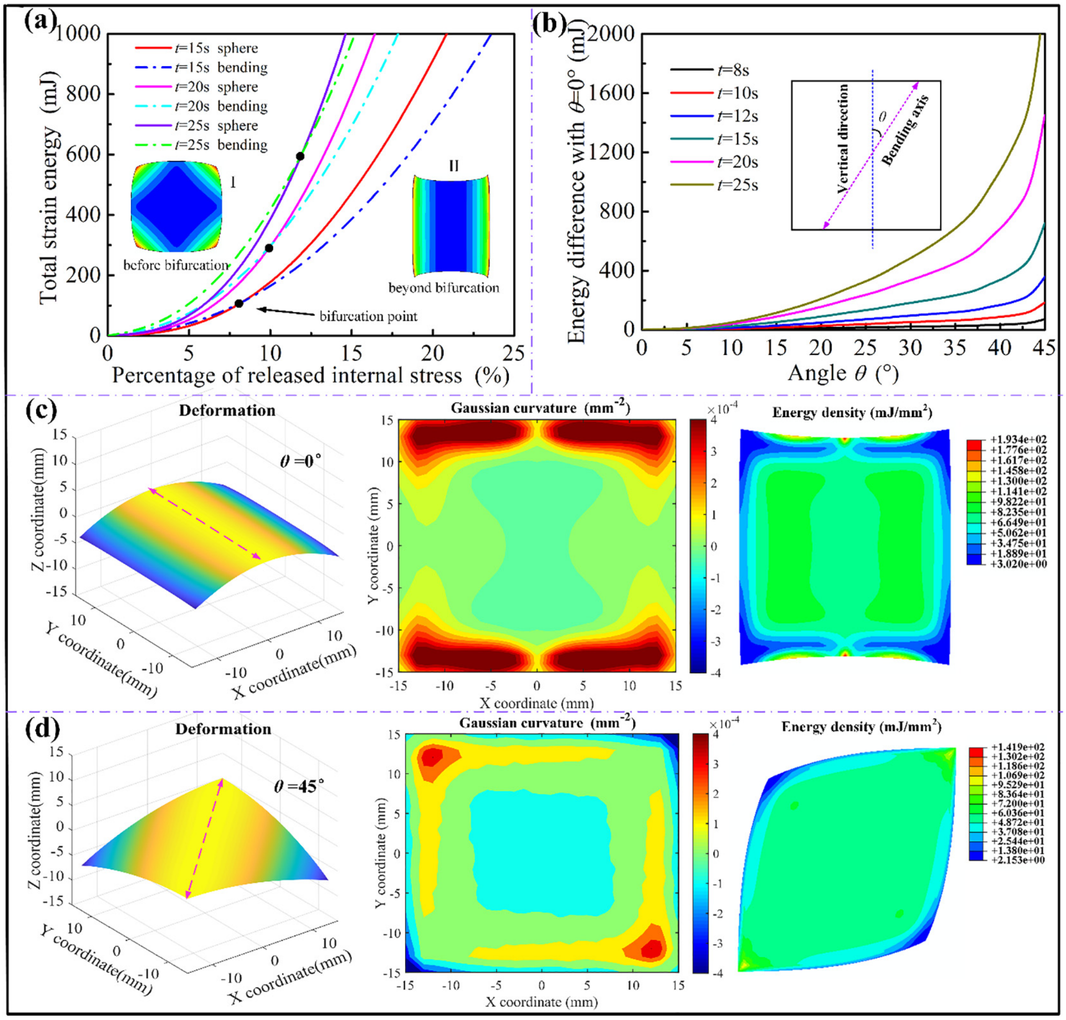

Fig. 4. Bifurcation due to the minimization of energy of the thin film. (a) The comparisons of the total strain energies as the cured samples deform into the (solid curves) spherical or (dashed curves) bending shapes. The horizontal axis shows the percentage of the internal stress released. The sample deforms into a spherical shape (inset I) initially and then changes to a bending shape (inset II) beyond the bifurcation point (black markers). (b) The variations of the total energy of the bending shape with respect to different axis $\theta = 0°$ to 45° for a square sample. The irradiation time varies from $t = 8$ to 25 s. The inset schematically shows the orientation of the bending axis. (c) The deformed shape of a rectangular sample bends with respect to the axis with $\theta = 0°$. Its Gaussian curvature distribution map shows large positive Gaussian curvature exists along the edges, corresponding to low energy density areas. (d) The deformed shape, Gaussian curvature and energy density of the rectangular sample bends with respect to the axis with $\theta = 45°$ are also shown. Energy differences induce shape-shifting of different bending modes.

when only a small portion of the internal stress is released. It means that the 2D cured thin shell will deform to a spherical shape with two equal main curvatures (inset I) when the deformation is small. As the internal stress releases more, the energy of the spherical shape increases faster than that of the bending shapes. Beyond a critical value 8.5% for $t = 15$ s, 10.5% for $t = 20$ s, and 12% for $t = 25$ s, the energies of the bending shapes are lower and the spherical shapes bifurcate into the bending shapes with two unequal primary curvatures (inset II).

To find the preferred bending axis, the total elastic energy of the deformed shape of a 2D square film versus the orientation angle θ of the bending axis is calculated for different irradiation times $t = 8$ s, 10 s, 12 s, 15 s, 20 s, 25 s as shown in Fig. 4b. The incident light intensity is 5 mW/cm^2. All of the elastic energies are subtracted by the elastic energy at $\theta = 0°$. It can be observed that all of the energies increase with the increase of the angle θ. Thus, the preferential bending of a square film is with respect to the axis with $\theta = 0°$, which agrees with the findings that the structure will bend with respect to the short axis [35,41,53].

To visualize the energy difference between bending shape with different bending axes, the deformed shape, Gaussian curvature distribution and energy density distribution of a rectangular film bending with respect to (1) the length direction ($\theta = 0°$), and (2) the diagonal direction ($\theta = 45°$) are plotted in Fig. 4c and d, respectively. The irradiation dose $D = 50$ mJ/cm^2. It can be seen that large and positive Gaussian curvatures exist along the edge (red regions), which corresponds to the low energy density areas (blue regions). It is the so-called "edge effect" that is investigated previously [41]. Large Gaussian curvatures indicate that bending is dominative over the stretching, and the elastic energy is reduced as a result. Many previous works have been done on the shape-shifting behaviors due to the edge effects [38–41,54,55]. "Edge effect" is a geometrical constraint that affects the deformation or stability of a structure. For a structure, the constraints near the edge are weaker than those at the center. Thus, the region near the edge can deform more freely and the energy density in the edge region is lower than that in the center. During the shape-shifting of the cured film, the energy density at the edge region is nearly 80% lower than that in the center, as shown in Fig. 4c (iii) and 4d (iii). The preferred bending shape is the one that minimizes its strain energy with a significant edge effect. The edge effect exists everywhere, such as the wrinkling of the leaves, flowers, or human skins [55]. In the growth of the leaves and flowers or the aging of the human skins, the structures are smooth and featureless at the center due to the strong constraints. But the stress is relaxed near the edge due to the fewer constraints. Thus, buckles appear at the edge to reduce the strain energy. The edge effect in both cases reduces the energy density along the edge and drives the bifurcation of the structures to a shape with lower energy. Another example is the morphological transition from mono- to bistable states due to the edge effect [54]. "Edge effect" is also observed and predicted using the developed model in other polygonal shapes like triangle, pentagon and hexagon as shown in Fig. S6 and Video S4.

3.5. Design of 3D structures using grayscale patterning

To form complex 3D structures, grayscale patterning is used in this section. The usage of grayscale light patterns allows the formation of in-plane graded materials with widely tunable mechanical properties. Thus various complex 3D structures can be formed by a single layer photopolymerization, which reduces the processing time and material cost significantly.

Fig. 5 shows the experimental and FE simulated deformed 3D shapes formed by the grayscale light patterns. A helical shape is generated by the anisotropic stress due to the aligned regions in Fig. 5a. By adjusting the grayscale patterns in a leaf, both symmetric and asymmetric 3D shapes can be formed (Fig. 5b and c). Using graded grayscale patterns in an annulus, a saddle shape can be created (Fig. 5d). Origami structures can also be generated by adjusting the grayscale patterns in the hinges (Fig. 5e and f). Comparing to the continuous outer boundary (Fig. 5g), the use of discrete boundary (Fig. 5h) can reduce the geometrical constraints and leads to the formation of a higher dome. Continuous changed grayscale pattern can also be applied to generate structures, like a flower (Fig. 5i).

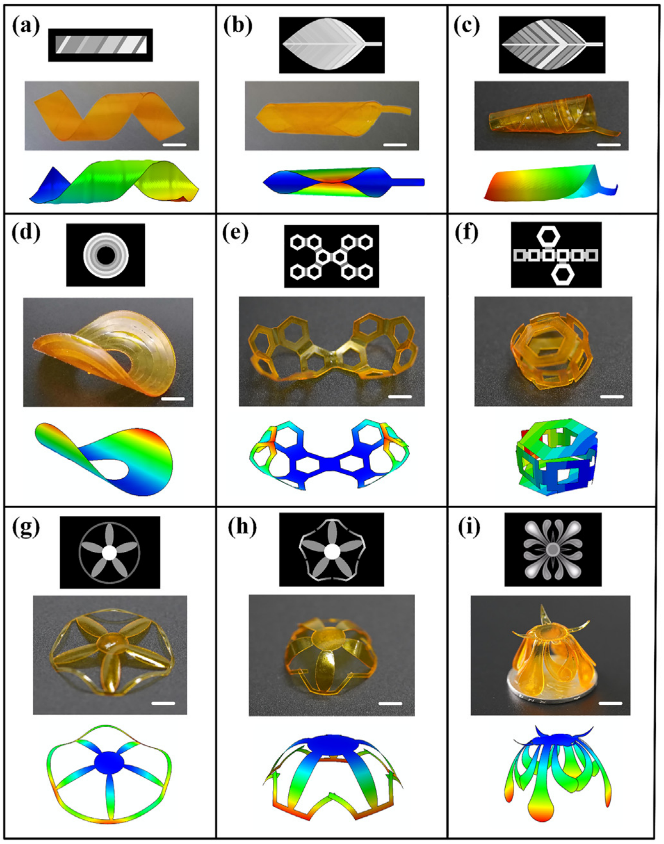

Fig. 5. Experimental and FE simulated results of the structures by FPP using grayscale light patterns. A helical shape (a), leaves (b, c), an annulus (d), origami structures (e, f), circles with inner patterns (g, h) and a flower (i) are formed. The corresponding grayscale light patterns are also shown. All of the scale bars are 5 mm.

3.6. Discussions

The shape-shifting is induced by the release of internal stress. During FPP, the material shrinks due to the formation of covalent bonds, which is generally undesirable in 3D printing as it causes shape distortion. Instead of trying to eliminate this phenomenon, we demonstrate that it can be utilized to create complex 3D structures, which are otherwise difficult to be fabricated. The proposed method has potential applications in areas such as microfabrication and soft robotics. It even suggests a new paradigm in product design, where the fabrication defects are taken into account. However, the resulting shape change is not reversible, which makes its active control difficult.

In principle, the shape changes automatically when the stress releases. However, the shape change is prohibited by the gravity and the adhesion due to the remaining resins. To enable the automatic shape change, we first use papers to absorb the resins. Some structures can then deform autonomously. But the shape changes of some other structures are prohibited by gravity, where a small actuation is needed to circumvent it. After the shape change, post-processing using the 405 nm light for around 2 min is conducted to fixed the shape. The effect of gravity and post-processing is further discussed in Section 8 in the Supplementary Materials.

It should be noted that photopolymerization is induced by both the radicals generated along with light penetration and propagation of radicals created by the interaction of light and monomers. In this work, the effect of the propagated radicals is neglected as the photoinitiator is efficient. However, the effect of the propagated radicals is worth further study [56–58].

Generally, photopolymerization is exothermic, and the released heat can trigger thermal strains. The thermal strain is neglected in this model. We have measured the temperature of the system. The temperature increase is 12 °C when irradiation time is 20 s. According to [59], the thermal expansion coefficient of PEGDA hydrogel is approximate $1.56 \times 10^{-4}\ \mathrm{K}^{-1}$. Thus, the thermal strain is around 0.2% for a temperature increase of 12 °C, which is one order less than the shrinkage strain.

The bending shape is determined by the edge effect. Alben et al. studied the preferential bending in thin rectangular bilayers. They concluded that the bending direction is determined by the existence of doubly curved regions at the curled edges, which lower the energy [41]. In our cases, the situation is more complicated due to the gradient on the *z* direction. But the same method can be used, and the preferential bending could be predicted by minimizing the energy.

4. Conclusions

In summary, we investigate the programmable shape change of a cured 2D pattern to a 3D structure driven by the release of internal stress built in the FPP process by a combination of experimental, theoretical and numerical methods. First, the relation between the internal stress of the cured sample and illumination dose is developed theoretically. Secondly, by using the discretized theoretical internal stress and Young's modulus along the thickness direction, FE simulations are established and conducted for the cured rectangles with various aspect ratios. Soft grippers are also designed. Thirdly, the bifurcation from a spherical to a bending shape in the shape transition is captured by minimizing the potential energy. Lastly, by using grayscale light patterns, various 3D complex geometries are formed and predicted.

The model takes into account the non-uniform distributed material properties and internal stress, and captures the bifurcation caused by the competition between bending and stretching. Similar to previous studies, edges with lower energy density and large Gaussian curvatures are found, which is the so-called “edge effect”. Based on the proposed model, both soft grippers using simple rectangle patterns and complex 3D structures using grayscale patterning are designed and demonstrated. This work provides a way to design and fabricate programmable 3D structures by tuning the 2D geometrical patterns and illumination doses.

Credit Author Statement

Jinqiang Wang: Methodology, Formal analysis, Investigation. **Ning Dai**: Conceptualization, Methodology, Supervision. **Chengru Jiang**: Methodology, Validation, Investigation. **Xiaoming Mu**: Methodology, Writing - Review & Editing. **Biao Zhang**: Formal analysis, Writing - Review & Editing. **Qi Ge**: Methodology, Supervision. **Dong Wang**: Writing - Review & Editing, Funding acquisition.

Declaration of Competing Interest

The authors declare that they have no known competing financial interests or personal relationships that could have appeared to influence the work reported in this paper.

Acknowledgment

D.W. acknowledges the support by grants from the National Natural Science Foundation of China (Grant No. 51905336) and the Shanghai Sailing Program from Shanghai Municipal Committee of Science and Technology (Grant No. 19YF1423000). N.D. acknowledges the support by grant from the National Natural Science Foundation of China (Grant No.51775273).

Appendix A. Supplementary data

Details on the experimental procedures, the manufacturing methods, the theoretical model, the FE analysis and related Videos are shown in the Supplementary Materials. Supplementary data to this article can be found online at [doi: https://doi.org/10.1016/j.matdes.2020.109381].

References

[1] S. Miyashita, et al., Robotic Metamorphosis by Origami Exoskeletons, Sci. Robot. 2 (10) (2017) eaao4369.
[2] T. van Manen, et al., Kirigami-enabled Self-folding Origami, Mater. Today 32 (2019) 59–67.
[3] Z. Zhao, et al., Origami by frontal photopolymerization, Sci. Adv. 3 (4) (2017) p. e1602326.
[4] A. Cangialosi, et al., DNA sequence–directed shape change of photopatterned hydrogels via high-degree swelling, Science 357 (6356) (2017) 1126–1130.
[5] L. Ionov, Biomimetic 3D self-assembling Biomicroconstructs by spontaneous deformation of thin polymer films, J. Mater. Chem. 22 (37) (2012) 19366–19375.
[6] Z. Chen, et al., Mechanical self-assembly of a strain-engineered flexible layer: wrinkling, rolling, and twisting, Phys. Rev. Appl. 5 (1) (2016), 017001, .
[7] D.P. Holmes, Elasticity and stability of shape changing structures, Curr. Opin. Colloid Interface Sci. 40 (2019) 118–137.
[8] V. Brunck, et al., Elastic theory of origami-based Metamaterials, Phys. Rev. E 93 (3) (2016), 033005, .
[9] E. Sharon, E. Efrati, The mechanics of non-Euclidean plates, Soft Matter 6 (22) (2010) 5693–5704.
[10] Y. Yang, M.A. Dias, D.P. Holmes, Multistable Kirigami for tunable architected materials, Phys. Rev. Mater. 2 (11) (2018) 110601.
[11] S. Janbaz, R. Hedayati, A. Zadpoor, Programming the shape-shifting of flat soft matter: from self-rolling/self-twisting materials to self-folding origami, Mater. Horiz. 3 (6) (2016) 536–547.
[12] A.R. Studart, Biologically inspired dynamic material systems, Angew. Chem. Int. Ed. 54 (11) (2015) 3400–3416.
[13] R. Elbaum, et al., The role of wheat awns in the seed dispersal unit, Science 316 (5826) (2007) 884–886.
[14] C. Dawson, J.F. Vincent, A.-M. Rocca, How pine cones open, Nature 390 (6661) (1997) 668–668.
[15] L. Huang, et al., Ultrafast digital printing toward 4D shape changing materials, Adv. Mater. 29 (7) (2017) 1605390.
[16] Y. Zhang, et al., 4D printing of a digital shape memory polymer with tunable high performance, ACS Appl. Mater. Interfaces 11 (35) (2019) 32408–32413.
[17] Z. Zhao, et al., 3D printing of complex origami assemblages for reconfigurable structures, Soft Matter 14 (39) (2018) 8051–8059.
[18] Z. Zhao, et al., Hydrophilic/hydrophobic composite shape-shifting structures, ACS Appl. Mater. Interfaces 10 (23) (2018) 19932–19939.
[19] Z. Zhao, H.J. Qi, D. Fang, A finite deformation theory of Desolvation and swelling in partially photo-cross-linked polymer networks for 3D/4D printing applications, Soft Matter 15 (5) (2019) 1005–1016.
[20] J. Wu, et al., Evolution of material properties during free radical Photopolymerization, J. Mech. Phys. Solid 112 (2018) 25–49.
[21] Z. Zhao, et al., Desolvation induced origami of Photocurable polymers by digit light processing, Macromol. Rapid Commun. 38 (13) (2017) 1600625.
[22] E. Siéfert, et al., Bio-inspired pneumatic shape-morphing elastomers, Nat. Mater. 18 (1) (2019) 24–28.
[23] J. Dervaux, et al., Shape transition in artificial tumors: from smooth buckles to singular creases, Phys. Rev. Lett. 107 (1) (2011), 018103, .
[24] A.S. Gladman, et al., Biomimetic 4D printing, Nat. Mater. 15 (4) (2016) 413–418.
[25] Y. Zhou, et al., Assembly pressure and membrane swelling in PEM fuel cells, J. Power Sources 192 (2) (2009) 544–551.
[26] A.A. Bauhofer, et al., Harnessing photochemical shrinkage in direct laser writing for shape morphing of polymer sheets, Adv. Mater. 29 (42) (2017) 1703024.
[27] Z. Ding, et al., Direct 4D printing via active composite materials, Sci. Adv. 3 (4) (2017), e1602890, .
[28] J. Kim, et al., Designing responsive buckled surfaces by halftone gel lithography, Science 335 (6073) (2012) 1201–1205.
[29] Q. Ge, et al., Active origami by 4D printing, Smart Mater. Struct. 23 (9) (2014), 094007, .
[30] A. Vitale, et al., A unified approach for patterning via frontal photopolymerization, Adv. Mater. 27 (40) (2015) 6118–6124.
[31] A. Vitale, J.T. Cabral, Frontal conversion and uniformity in 3D printing by Photopolymerisation, Materials 9 (9) (2016) 760–773.
[32] G.G. Stoney, The tension of metallic films deposited by electrolysis, Proce.Royal Soci. Lond. Seri. A, Contain.Pap. Math. Phys. Charact 82 (553) (1909) 172–175.
[33] L. Freund, Substrate curvature due to thin film mismatch strain in the nonlinear deformation range, J. Mech. Phys. Solid 48 (6–7) (2000) 1159–1174.

[34] D.P. Holmes, et al., Bending and twisting of soft materials by non-homogenous swelling, Soft Matter 7 (11) (2011) 5188–5193.

[35] M. Pezzulla, et al., Geometry and mechanics of thin growing bilayers, Soft Matter 12 (19) (2016) 4435–4442.

[36] A.M. Abdullah, et al., Self-folded gripper-like architectures from stimuli-responsive bilayers, Adv. Mater. 30 (31) (2018) 1801669.

[37] A.M. Abdullah, et al., Mismatch strain programmed shape transformation of curved bilayer-flexible support assembly, Extreme Mech. Lett. 7 (2016) 34–41.

[38] A.M. Abdullah, P.V. Braun, K.J. Hsia, Bifurcation of self-folded polygonal bilayers, Appl. Phys. Lett. 111 (10) (2017) 104101.

[39] C. Modes, M. Warner, Shape-programmable materials, Phys. Today 69 (1) (2016) 32–38.

[40] I.S. Chun, et al., Geometry effect on the strain-induced self-rolling of semiconductor membranes, Nano Lett. 10 (10) (2010) 3927–3932.

[41] S. Alben, B. Balakrisnan, E. Smela, Edge effects determine the direction of bilayer bending, Nano Lett. 11 (6) (2011) 2280–2285.

[42] M.G. Hennessy, et al., Controlling frontal photopolymerization with optical attenuation and mass diffusion, Phys. Rev. E 91 (6) (2015) 062402.

[43] J.T. Cabral, et al., Frontal photopolymerization for microfluidic applications, Langmuir 20 (23) (2004) 10020–10029.

[44] M. Belk, et al., Frontal photopolymerization with convection, J. Phys. Chem. B 107 (37) (2003) 10292–10298.

[45] J.A. Warren, J.T. Cabral, J.F. Douglas, Solution of a field theory model of frontal photopolymerization, Phys. Rev. E 72 (2) (2005) 021801.

[46] H. Lee, et al., Prescribed pattern transformation in swelling gel tubes by elastic instability, Phys. Rev. Lett. 108 (21) (2012) 214304.

[47] H. Lee, N.X. Fang, Micro 3D printing using a digital projector and its application in the study of soft materials mechanics, JoVE (Journal of Visualized Experiments) (69) (2012) e4457.

[48] A.J. Keefe, N.D. Brault, S. Jiang, Suppressing surface reconstruction of superhydrophobic PDMS using a superhydrophilic zwitterionic polymer, Biomacromolecules 13 (5) (2012) 1683–1687.

[49] M. Jin, et al., Super-hydrophobic PDMS surface with ultra-low adhesive force, Macromol. Rapid Commun. 26 (22) (2005) 1805–1809.

[50] D.S. Kim, et al., Fabrication of PDMS micro/nano hybrid surface for increasing hydrophobicity, Microelectron. Eng. 86 (4–6) (2009) 1375–1378.

[51] D.J. Glugla, et al., Rigid origami via optical programming and deferred self-folding of a two-stage photopolymer, ACS Appl. Mater. Interfaces 8 (43) (2016) 29658–29667.

[52] J. Wang, et al., Modeling and application of planar-to-3D structures via optically programmed frontal Photopolymerization, Adv. Eng. Mater. 21 (5) (2019) 1801279.

[53] H. Yang, et al., A chemo-mechanical model of Lithiation in silicon, J. Mech. Phys. Solid 70 (2014) 349–361.

[54] Z. Chen, et al., Nonlinear geometric effects in mechanical Bistable morphing structures, Phys. Rev. Lett. 109 (11) (2012) 114302.

[55] M. Marder, R.D. Deegan, E. Sharon, Crumpling, buckling, and cracking: elasticity of thin sheets, Phys. Today 60 (2) (2007) 33–38.

[56] J.-P. Fouassier, Photoinitiation, photopolymerization, and photocuring: fundamentals and applications, Hanser, 1995.

[57] J.-T. Lin, et al., Modeling the kinetics, curing depth, and efficacy of radical-mediated Photopolymerization: the role of oxygen inhibition, viscosity, and dynamic light intensity, Front. Chem. 7 (13) (2019) 00760.

[58] J.-T. Lin, D.-C. Cheng, Modeling the efficacy profiles of UV-light activated corneal collagen crosslinking, PLoS One 12 (4) (2017) p. e0175002.

[59] Q. Wang, et al., Lightweight mechanical metamaterials with tunable negative thermal expansion, Phys. Rev. Lett. 117 (17) (2016) 175901.